

Article

Numerical Simulation of Acid Gas Distribution and Corrosion Characteristics in Connecting Pipe of Lean/Rich Amine Heat Exchanger

Zeyang Shi¹, Jianjun Lv², Zhipeng E², Peixu Wei¹, Yukuan Gu¹, Yuge Li³, Wenming Song³, Yuan Yan¹, Liping Wei^{1,4,*} and Jun Hu^{1,4} 

¹ School of Chemical Engineering, Northwest University, Xi'an 710069, China

² Petro China Southwest Oil & Gasfield Company, Chengdu 610031, China

³ Machinery Industry Shanghai Lanya Petrochemical Equipment Inspection Institute Co., Ltd., Shanghai 201518, China

⁴ Youth Innovation Team of Shaanxi Universities, Xi'an 710069, China

* Correspondence: weiliping@nwu.edu.cn



Citation: Shi, Z.; Lv, J.; E, Z.; Wei, P.; Gu, Y.; Li, Y.; Song, W.; Yan, Y.; Wei, L.; Hu, J. Numerical Simulation of Acid Gas Distribution and Corrosion Characteristics in Connecting Pipe of Lean/Rich Amine Heat Exchanger. *Coatings* **2022**, *12*, 1460. <https://doi.org/10.3390/coatings12101460>

Academic Editor: Paweł Nowak

Received: 31 August 2022

Accepted: 29 September 2022

Published: 3 October 2022

Publisher's Note: MDPI stays neutral with regard to jurisdictional claims in published maps and institutional affiliations.



Copyright: © 2022 by the authors. Licensee MDPI, Basel, Switzerland. This article is an open access article distributed under the terms and conditions of the Creative Commons Attribution (CC BY) license (<https://creativecommons.org/licenses/by/4.0/>).

Abstract: In the high sulfur natural gas purification unit, the connecting pipe of a lean/rich amine heat exchanger is extremely susceptible to corrosion due to the acid gas and amine liquid condition. This work numerically investigated the gas–liquid flow and corrosion of the real-scale connecting pipeline with two horizontal sections, one vertical section and four elbow sections. The effect of acid gas holdup on the gas–liquid flow pattern, distribution of velocity and pressure, and corrosion rate was investigated using an experimental validated model. With an increase in the acid gas fraction from 0.03 to 0.12, the flow pattern of the horizontal section changes from bubbly flow to a stratified flow in the horizontal section, while the flow pattern of the vertical section and elbow section keeps bubbling, and the proportion of gas bubbles increases in the vertical section and all elbow sections. The maximum pressure gradient was observed on the top of the horizontal section. The most serious corrosion section was found out on the outlet of the first elbow section where the gas liquid flow starts to stratify, which is consistent with the measured minimum wall thickness. A solution measure for anti-corrosion acid gas in the pipeline was proposed by adding a bifurcated pipe to separate the acid gas in the first horizontal section. The accumulated acid gas was effectively thrown out from the outlet of the bifurcated pipe. This method provides a promising way to eliminate the acid gas in the pipe and avoid forming stratified flow, which is helpful for prolonging the service life of the pipe.

Keywords: flow pattern; gas phase distribution; pipeline corrosion; bifurcated pipe; simulation

1. Introduction

Natural gas purification is a necessary unit for the absorption of acid gas and producing clear natural gas. With the operation of the natural gas purification process, the content of medium in the purification system has changed in the conditions of high-pressure difference, high temperature of amine liquid and the increase in water content. The corrosive medium $\text{CO}_2\text{-H}_2\text{S-H}_2\text{O}$, $\text{R}_2\text{NH-H}_2\text{S-CO}_2\text{-H}_2\text{O}$, thermally stable salts, Cl^- , polluted impurities, etc. tend to cause local corrosion, cracking, etc. The corrosive medium will cause a certain degree of corrosion to the inner wall of the pipeline, and pipe fittings wear and tear can even cause equipment failure in severe cases [1–5]. Corrosion is the main damage mode of most pressure vessels and pipelines, and improving corrosion resistance is crucial for pipelines [6–10]. Corrosion will damage the metal surface and then cause the pipeline to fail due to corrosion and even cause vicious accidents such as leakage or explosion, which will bring serious hidden dangers to the environment, enterprise production, and people's property and life safety [11–13].

According to the pipeline corrosion data provided by the factory [14–17], the corrosion morphology of the connecting pipe of a lean/rich amine heat exchanger includes fluid erosion and acid gas corrosion for the corrosion failure of the connecting pipe. The corrosion of pipelines is usually localized corrosion, and its distribution has certain regularity, which is often affected by the corrosive medium, the geometry of the pipeline, and the flow velocity and flow pattern in the phase [18]. One widely used acid gas absorption medium of the purification unit is N-methyldiethanolamine (MDEA), which has low vapor pressure, thermal degradation rate, and corrosion rate [19,20]. However, the acid gas solubility in the MDEA is greatly affected by the operation temperature. The acid gas solubility decreases with the increase in temperature. When saturated MDEA solution flows into the connecting pipe of the heat exchanger, its temperature will increase and outflow acid gas, further forming a two-phase flow of acid gas and MDEA solution. The gas–liquid two-phase flow affects the flow and corrosion behavior. The basic flow and corrosion characteristics have not been obtained due to the limited investigation method.

Many scholars have carried out scientific research on two-phase flow pipeline corrosion [21,22], hoping to control and reduce the loss caused by corrosion to the pipeline and improve the service life of the pipeline by studying the corrosion characteristics of the pipeline in different media. Zhang et al. [23] analyzed the fluid–structure coupling characteristics of gas–liquid two-phase flow corrosion pipelines and obtained the position of the maximum principal stress on the pipeline as well as the maximum principal stress under two-way fluid–structure coupling and one-way fluid–structure coupling. Wang et al. [24] studied the flow-induced vibration characteristics of gas–liquid two-phase flow in the pipeline. Feng et al. [25] investigated the effect of iron ions in evaluating the corrosion status of buried steel pipelines and concluded that iron ions significantly affect the accuracy of potential measurement, thereby affecting the corrosion status of pipelines. Iftikhar and Rahuma [26] proposed the challenges and mitigation strategies in the field of pipeline corrosion. Kumar et al. [27] studied the corrosion of cathodic protected steel pipelines under alternating current and compared the alternating current corrosion performance of different pipeline steel grades. Paolinelli et al. [28] carried out corrosion prediction for gas–liquid two-phase flow and estimated the gas–liquid flow mass transfer rate by Chilton–Colburn analogy and near-wall eddy diffusion distribution. Yang et al. [29] studied the corrosion behavior of 20 # steel under water and CO₂. Peng [30] provided a new hybrid algorithm model for multiphase flow pipeline corrosion rate prediction. Li [31] used the Peclet quasi-number to calculate the dispersion coefficient and also used the dispersion coefficient to accurately correct the mass transfer coefficient in the electrochemical corrosion mass transfer model.

There are few mathematical models that relate gas–liquid flow to the corrosion characteristics of the lean/rich amine liquid heat exchanger, and the impact of gas–liquid flow on corrosion behavior is still an open question. The work focuses on the gas–liquid flow process in a typical gathering and transportation system pipeline of a gas field and tries to obtain the corrosion characteristic under the acid gas and amine flow. An experimentally validated CFD numerical simulation method is applied to study the gas–liquid erosion characteristics of the connecting pipes of the lean-rich amine–liquid heat exchanger. Typical working conditions have been investigated in terms of flow and corrosion characteristics. An anti-corrosion method of adding bifurcated pipe has been proposed and evaluated by numerical simulation. This work provides reference for pipeline design and maintenance.

2. Physical Model and Numerical Method

2.1. Physical Model

The numerical simulation in this paper is carried out for the lean/rich amine heat exchanger in an oil and gas field. A full-scale physical model was built according to actual pipeline. The nominal diameter of the pipeline is 1000 mm, and 90° vertical-upward and vertical-downward elbows 1.5 times the nominal diameter are adopted. The detailed dimensions are shown in Figure 1. The pipe is meshed by a hexahedron structure. The grid

at the elbow is locally refined. The naming of each part of the pipeline and the location of measuring points are shown in Figure 2.

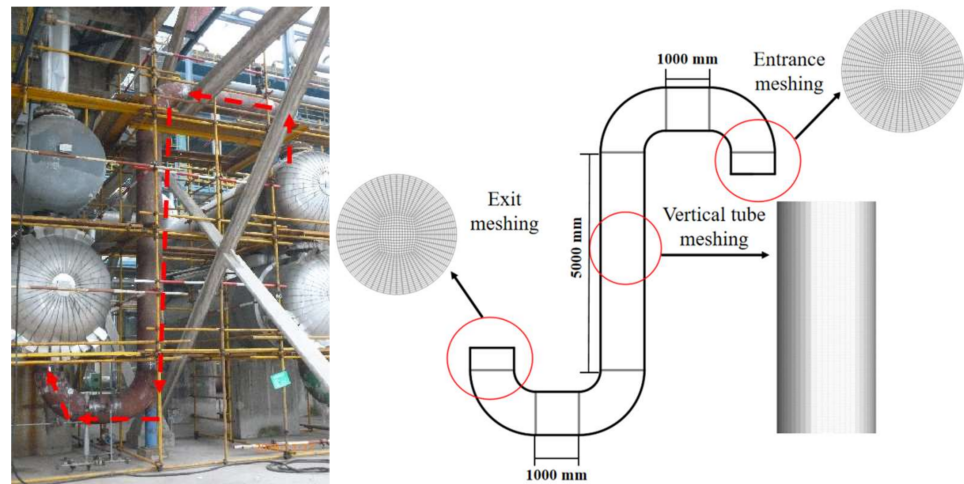


Figure 1. Full-scale model and mesh generation of the connecting pipe of lean/rich amine heat exchanger.

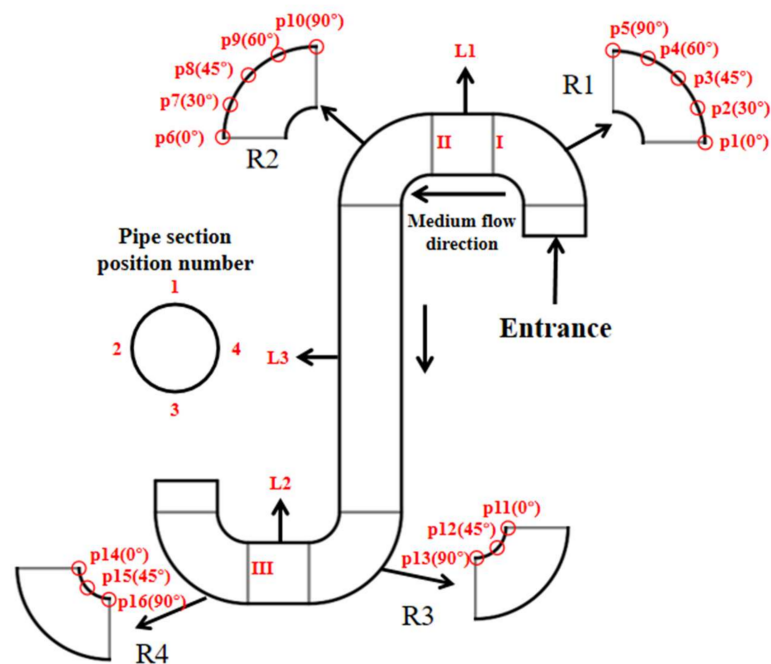


Figure 2. Section definition of the connecting pipe, R1–R4: elbow section; L1 and L2: horizontal section; L3 vertical section; I–III: cross-section; 1–4: position number of the cross-section.

2.2. Numerical Method

The volume of fluid (VOF) method was used to simulate the gas–liquid two-phase elbow flow [32]. This method solves the momentum equation and tracks the volume fraction of fluid in the control volume. This method is a surface-tracking method based on a fixed Euler grid. The VOF model is suitable for the premise that two or more fluids (or phases) do not mix with each other, and this model can be used when one or more immiscible fluid interfaces need to be obtained. In the VOF model, different fluid components share a set of momentum equations, and the phase interface of each computational unit can be tracked by introducing variable phase volume fractions. To study the corrosion of acid gas and amine liquid with different volume fractions in the pipeline, the VOF model is used for numerical simulation in this study [33–35]. The continuity equation, momentum

equation and volume fraction equation used in the calculation are shown in Appendix A (Appendix A.1) [36].

Many scholars have obtained equation solutions by studying the numerical methods of partial differential equations: Savović et al. [37] studied the nature and process of radon transport from underground soil to buildings and obtained the solution of the relevant transfer equation using the Explicit Finite Difference Method (EFDM). Zhou et al. [38] studied the application of wavelet theory to solve the numerical value of partial differential equations and proposed an adaptive algorithm for solving nonlinear partial differential equations—the Wavelet Optimal Finite Difference Method. Groza et al. [39] proposed a numerical method for solving polynomial partial differential equations in two independent variables. Li et al. [40] mainly studied the Finite Difference Method (FDM), the Finite Element Method (FEM) and the spectral method of Fractional Partial Differential Equations (FPDE). Yavneh et al. [41] established a Multilevel Nonlinear Method (MNM) for the numerical solution of nonlinear partial differential equations. They demonstrated that the advantages of two classical multi-grid methods can be combined to solve nonlinear problems.

At present, the most widely used discrete method in CFD software is the Finite Volume Method (FVM) [42–47]. Based on the experience of predecessors, the discretization scheme of the VOF equation is summarized in Appendix A (Appendix A.2). The gas–liquid flow in the pipeline is a typical turbulent flow. The standard $k - \varepsilon$ model is applied, and the control equations are shown in Appendix A (Appendix A.3). Fluent software was applied in solving the control equations.

The research mainly focuses on the corrosion of pipelines by gas–liquid two-phase flow, in which acid gas is selected for the gas phase and MEDA solution is selected for the liquid phase. Specifically, the liquid phase inlet velocity is 0.67 m/s, the gas phase volume fraction is 0.1, the liquid phase density is 1039 kg/m³, the gas phase density is 7.76 kg/m³, the liquid phase viscosity is 0.0103 kg/m·s⁻¹, the gas phase viscosity is 1.2×10^{-5} kg/m·s⁻¹, the liquid phase surface tension is 0.007 N/m, and the surface roughness is 0.0046 mm.

2.3. Grid Independent Test

To ensure the calculation accuracy and prevent too many grids from occupying a lot of computing resources, the influence of the number of grids on the pressure drop at the inlet and outlet of the pipeline is independently verified, and the appropriate number of grids is determined. Using multiple sets of grid trial calculation, transient calculation, and statistical pipeline simulation for 13 s, the relationship between the pressure drop at the inlet and outlet of the pipeline and the grid is shown in Figure 3. It is found that the pressure drop tends to be stable after the number reaches 1.7 million, and it is considered that after that, the number of meshes has no effect on the results. Since all elbow models are of similar size, this number of meshes is used uniformly. Therefore, the total number of pipeline meshes is selected as 1,956,892.

2.4. Model Validation

To validate the present numerical model, the flow pattern of air–water two-phase flow in five typical conditions was recorded in a reduced-scale experimental setup. The gas–liquid two-phase flow experimental device is shown in Figure 4. The experimental pipeline is composed of a horizontal pipe with a reduced-scale inner diameter of 30 mm. The whole experimental setup is equipped with flowmeter, pressure gauge and thermometer for the measurement of two-phase flow parameters. The experimental system is roughly divided into three parts: gas–liquid mixing area, high-speed photography area and gas–liquid separation area. The gas phase discharged by the compressor and stored in the gas tank is mixed with the liquid phase provided by the water pump and flows into the pipeline at a certain flow rate. The experimental setup sets up a float flowmeter and flowmeter, respectively, before the gas–liquid mixing flow equalization section to monitor

the gas–liquid two-phase flow data. A pressure gauge and a thermometer are set to monitor the pressure and temperature data of the fluid flow in the pipeline. When the fluid enters the transparent chamber along the pipeline, the bubble distribution in the pipeline is photographed by a high-speed camera for comparison with the simulated data. The two-phase flow is separated and recovered by the gas–liquid separator.

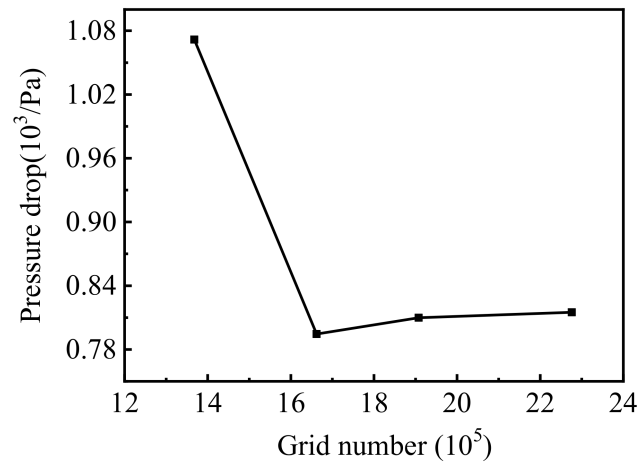


Figure 3. Variation of pressure drop with refinement of the grid.

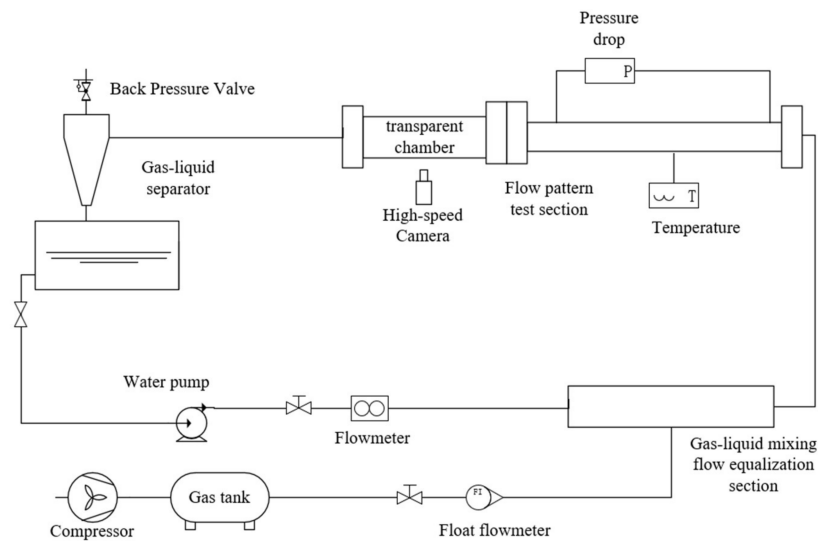


Figure 4. Flow process diagram of experimental setup.

The horizontal pipeline model is built, as shown in Figure 5. The distribution of air bubbles in water flow was simulated. The comparison between the experimental and simulated results is shown in Figure 6. Both the simulation results and the experiments capture the bubble distribution in the tube. The simulation results are basically consistent with the experimental results, and with the increase in the gas volume fraction, the number of bubbles in the tube also increases. At the same time, after the bubbles are generated, they are enriched to the top of the pipe wall, and a bubble enrichment area is formed at the upper wall of the pipe.

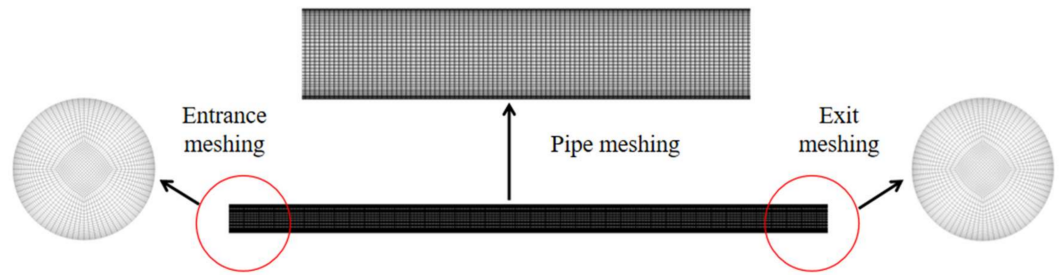


Figure 5. Grid of horizontal pipe according to the experiment.

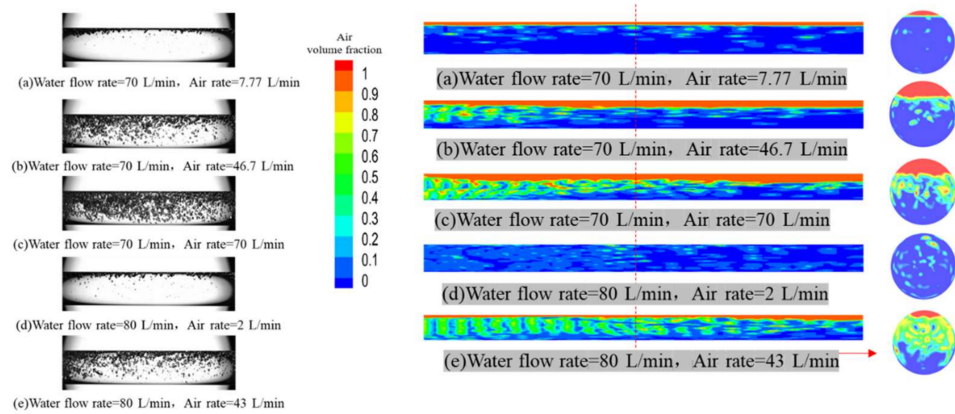


Figure 6. Comparison of gas-liquid phase distribution of simulation and experiment.

The gas phase distribution section is taken from the line drawn in the middle of the tube, and the thickness of the gas film in the horizontal tube after the experiment and simulation is compared, as shown in Figure 7 (relative error = 13.1%). The simulation results are roughly the same as the experimental results. As the gas flow rate increases, the thickness of the gas film increases, and the bubbles in the water phase also increase gradually. Since the density of air is much smaller than that of water, many bubbles will attach to the upper half wall of the pipe, the fluid in the pipe scours the upper wall of the pipe to a greater extent than the lower wall, so the corrosion of the upper wall of the pipe is more obvious.

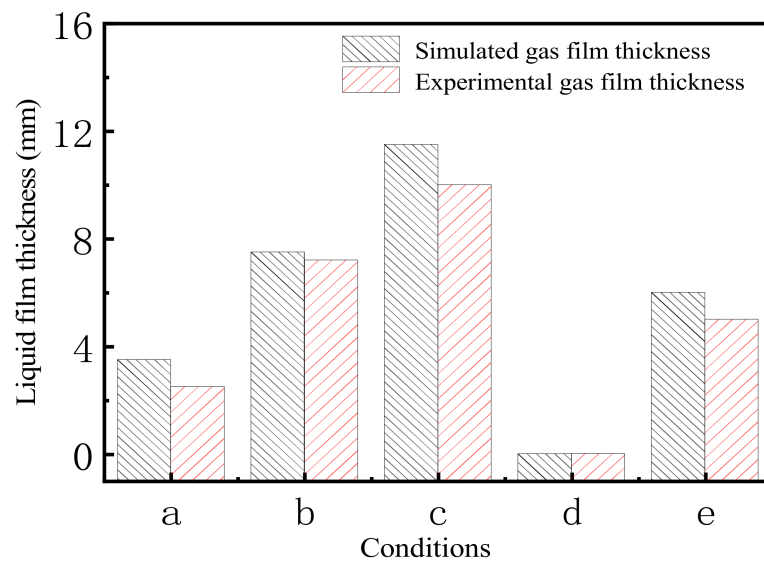


Figure 7. Comparison of simulated gas film thickness and experimental data.

3. Results and Discussion

Flow patterns have different pressure, flow characteristics, heat transfer characteristics and corrosion characteristics. The calculation of corrosion characteristics without considering the change of flow pattern is rough and unreliable. It can be said that flow pattern is the basis of two-phase flow research [48]. The calculation of corrosion rate is greatly related to the division of flow pattern and related fluid parameters, so it is necessary to judge the flow pattern in the pipeline before solving the model.

3.1. Flow Pattern

The gas phase distribution of the acid gas with the inlet velocity of 0.67 m/s and the volume fraction of 0.1 in the pipeline is shown in Figure 8. It can be seen that many bubbles are dispersed in each part of the tube, and bubbles are enriched at the upper walls of the L1 and L2 sections. As the calculation time increases, the bubbles generally accumulate near the upper wall of L1. A huge bubble enrichment area on the upper wall of L1 and an obvious stratified flow is formed. There is also a small amount of bubble enrichment in the upper wall part of L2; there is bubble dispersion at the center L3 of the pipe, which is a typical bubbly flow. Therefore, the flow pattern of the connecting pipe of a lean/rich amine heat exchanger is complex. The horizontal section of L1 and L2 is stratified flow, and the elbow sections and the vertical section of L3 are bubbly flow. The gas–liquid bubbly flows into the first elbow section of R1, and the acid gas is separated under the effect of centrifugation and buoyancy forces, and then, it is enriched near the top wall of L1. The evolution of flow pattern produces a complex interaction of gas–liquid, continued variation of local gas holdup, and huge fluctuations of pressure and velocity. These factors may further affect the pipe wall corrosion behavior.

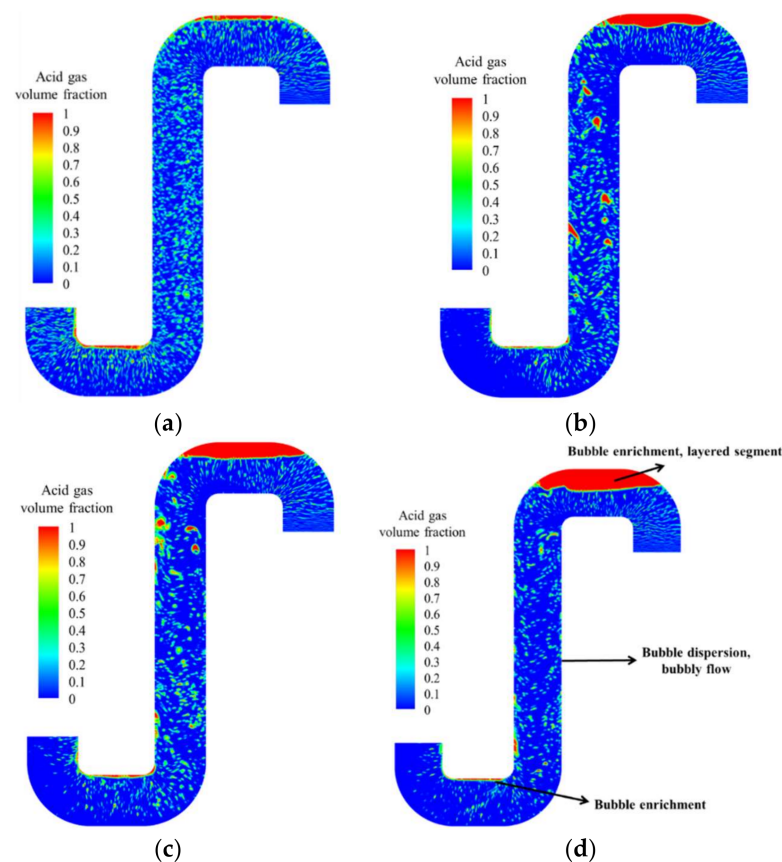


Figure 8. Gas phase distribution for gas volume fraction 0.1, $u = 0.67$ m/s. (a) $t = 1.00$ s (b) $t = 3.65$ s. (c) $t = 6.70$ s (d) $t = 11.0$ s.

3.2. Effect of Inlet Gas Holdup

3.2.1. Pipeline Pressure Distribution

The gas holdup has great effect on the flow process [49]. The gas phase distribution of the acid gas in the pipe is calculated transiently under conditions of inlet acid gas phase volume fraction of 0.03, 0.05, 0.07, 0.1 and 0.12. The pressure map is shown in Figure 9. It can be seen from Figure 8a that the pressure at the upper wall of L1 and the elbows of R3 and R4 is larger than in the other positions, such as the elbows of R1 and R2. The pressure increases with the increase in acid gas fraction. The maximum pressure position is located at L2. For the upper wall part of the horizontal section L1, the area of the low-pressure increases with the increase in the acid gas volume fraction. In the condition of acid gas volume fraction 0.03, the low-pressure mainly exists on the inner wall of the elbows R1 and R2. As the volume fraction of acid gas increases, the low-pressure expands from the inner wall area of the elbows R1 and R2 to the upper part of the pipeline. The increasing acid gas fraction cause a larger pressure drop, as shown in Figure 10. This is mainly attributed to the increased gas–liquid interphase resistance induced by the increasing acid gas fraction. When the acid gas volume fraction is 0.07, the corresponding maximum pressure gradient value is the smallest; when the gas volume fraction is 0.03, the pressure drop is the smallest; when the gas volume fraction is 0.1, the pressure drop and the maximum pressure gradient value are the largest.

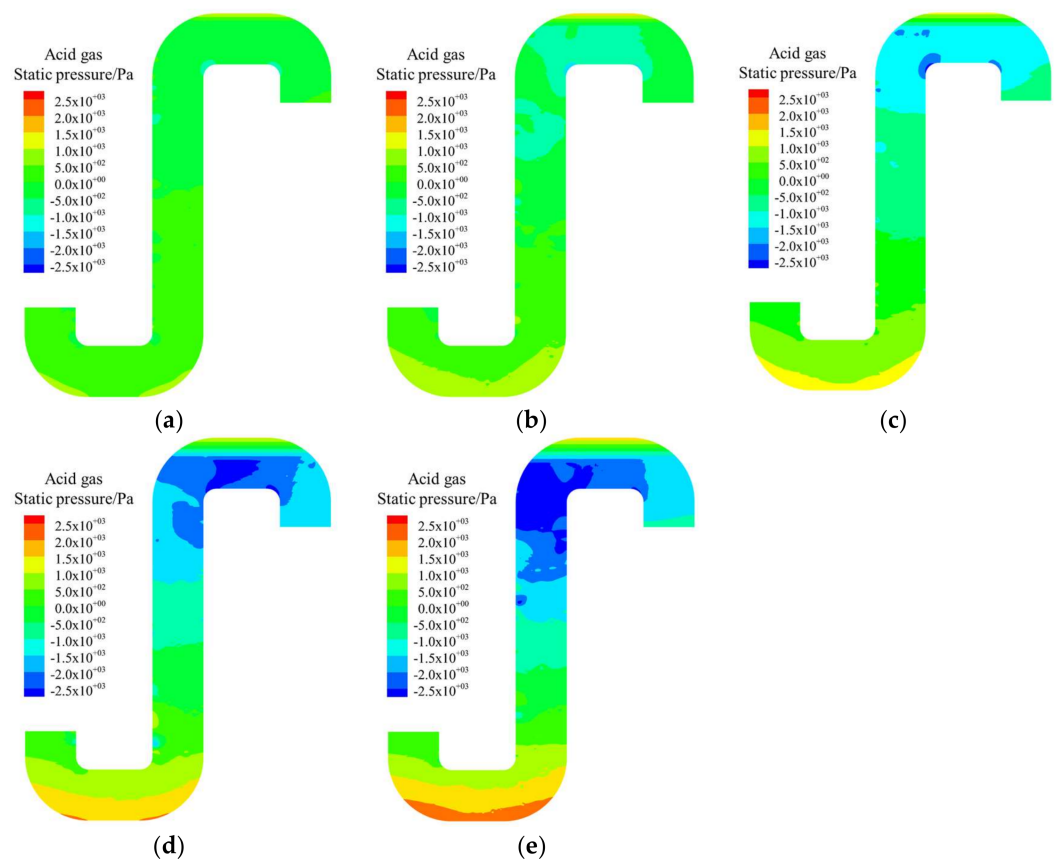


Figure 9. Pressure distribution under variable inlet gas fraction conditions ($t = 11$ s, $u = 0.67$ m/s). (a) $\alpha = 0.03$ (b) $\alpha = 0.05$ (c) $\alpha = 0.07$. (d) $\alpha = 0.1$ (e) $\alpha = 0.12$.

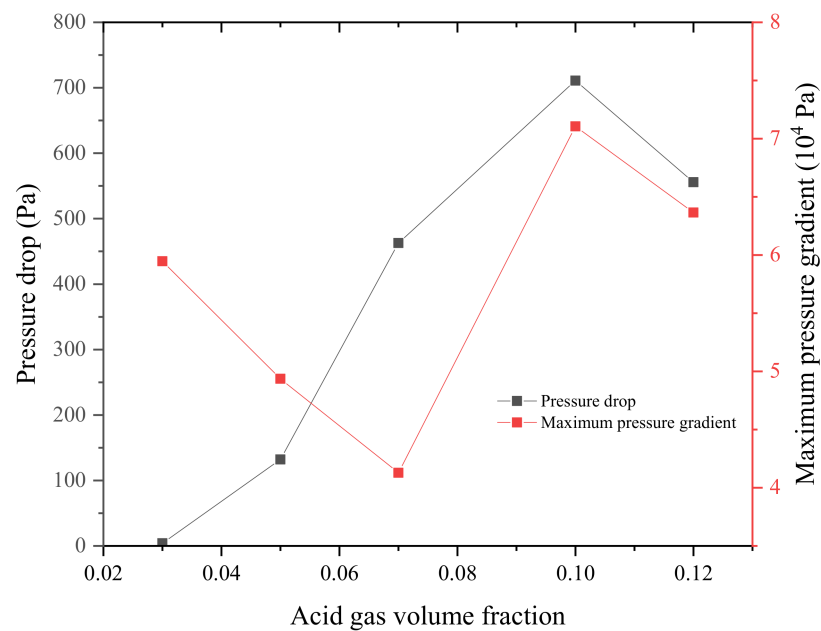


Figure 10. Pressure drop under variable inlet gas fraction conditions.

3.2.2. Velocity Distribution

The influence of the inlet gas holdup of the connecting pipe of the poor-rich amine liquid heat exchanger on the velocity in the pipe is studied, and the pipeline velocity distribution cloud map and the pipeline velocity vector diagram are shown in Figure 11. The velocity vector diagram can clearly observe the flow line of the acid gas in the pipeline. First, uniformly select the velocity comparison under the range of maximum velocity of 8 m/s. When the acid gas volume fraction is 0.03, there are high flow velocity areas on the inner walls of elbows R1, R2, R3, and R4. With the increase in the gas volume fraction, the velocity in the tube increases, the area of high flow velocity increases, and the area of low flow velocity decreases. The high flow velocity area in the pipe is expanded from the inner wall area of the four elbows to the upper wall surface of L1, L2 and part of the area of L3, and the position of the maximum velocity in the pipe is at the inner wall of the pipe elbow R4. Figure 12 plots the relationship between the acid gas volume fraction and the maximum velocity and the maximum velocity gradient in the tube. When the gas volume fraction is 0.03, the maximum velocity value in the tube is the smallest, and the maximum velocity gradient value is the smallest; when the gas volume fraction is 0.1, the maximum velocity value in the tube is the largest; when the gas volume fraction is 0.12, the maximum velocity gradient value in the tube is the largest.

3.2.3. Bubble Distribution

The gas phase distribution of acid gas was simulated by the Fluent VOF model; the gas phase volume fraction was set to five operating conditions of 0.03, 0.05, 0.07, 0.1, and 0.12; and the cloud diagram of the gas phase distribution of acid gas was made as shown in Figure 13. It can be seen from the cloud diagram that the volume fraction of the gas keeps increasing, and the acid gas accumulates in a larger volume on the upper wall of the pipeline. It can be seen from the section at L1 that the proportion of the acid gas increases. When the volume fraction is 0.12, the proportion of the acid gas is approximately half. With the increase in the volume fraction of acid gas, the bubble-like flow pattern of the pipeline becomes more pronounced, the distribution of bubbles at the outlet of the pipeline increases, the distribution of bubbles in various parts of the pipeline also increases, and the proportion of bubbles in each section also increases. In addition, the acid gas has an impact on the pipeline, the corrosion of the wall also increases accordingly, and the gas distribution in the simulated tube is consistent with the gas distribution in the literature [28]. This is

because in the gas–liquid flow in the tube, the air bubbles will be dispersed in the tube along with the flow of the fluid in the tube. Since the acid gas density is much smaller than that of the MEDA solution, with the increase in time, the acid gas will be greatly enriched in the upper wall part of the pipeline L1. For the bubble enrichment area on the upper wall of the pipeline L1, specific anti-corrosion measures need to be implemented to prolong the service life of the pipeline.

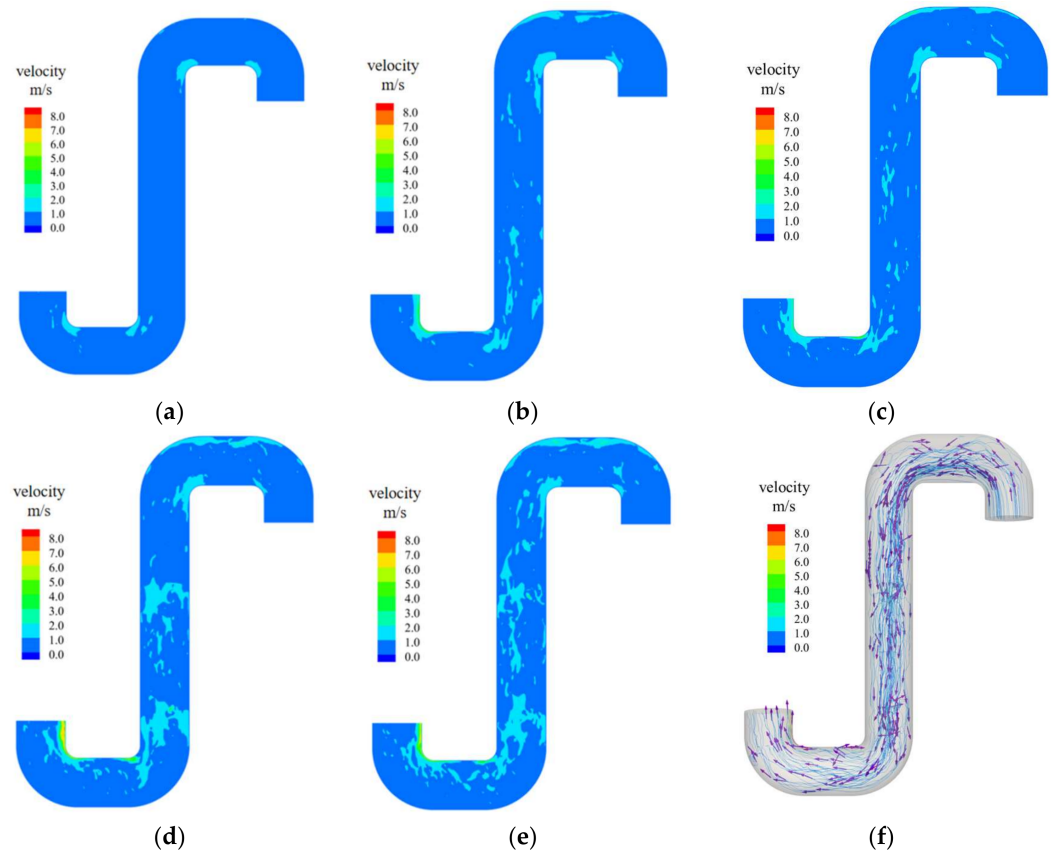


Figure 11. Velocity distribution under different inlet gas volume fraction conditions ($t = 11$ s, $u = 0.67$ m/s). (a) $\alpha = 0.03$ (b) $\alpha = 0.05$ (c) $\alpha = 0.07$. (d) $\alpha = 0.1$ (e) $\alpha = 0.12$ (f) $\alpha = 0.1$.

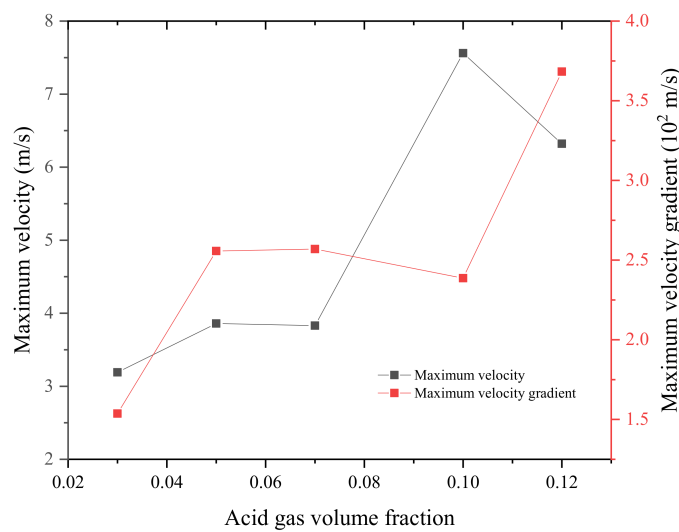


Figure 12. Maximum velocity under variable acid gas volume fractions.

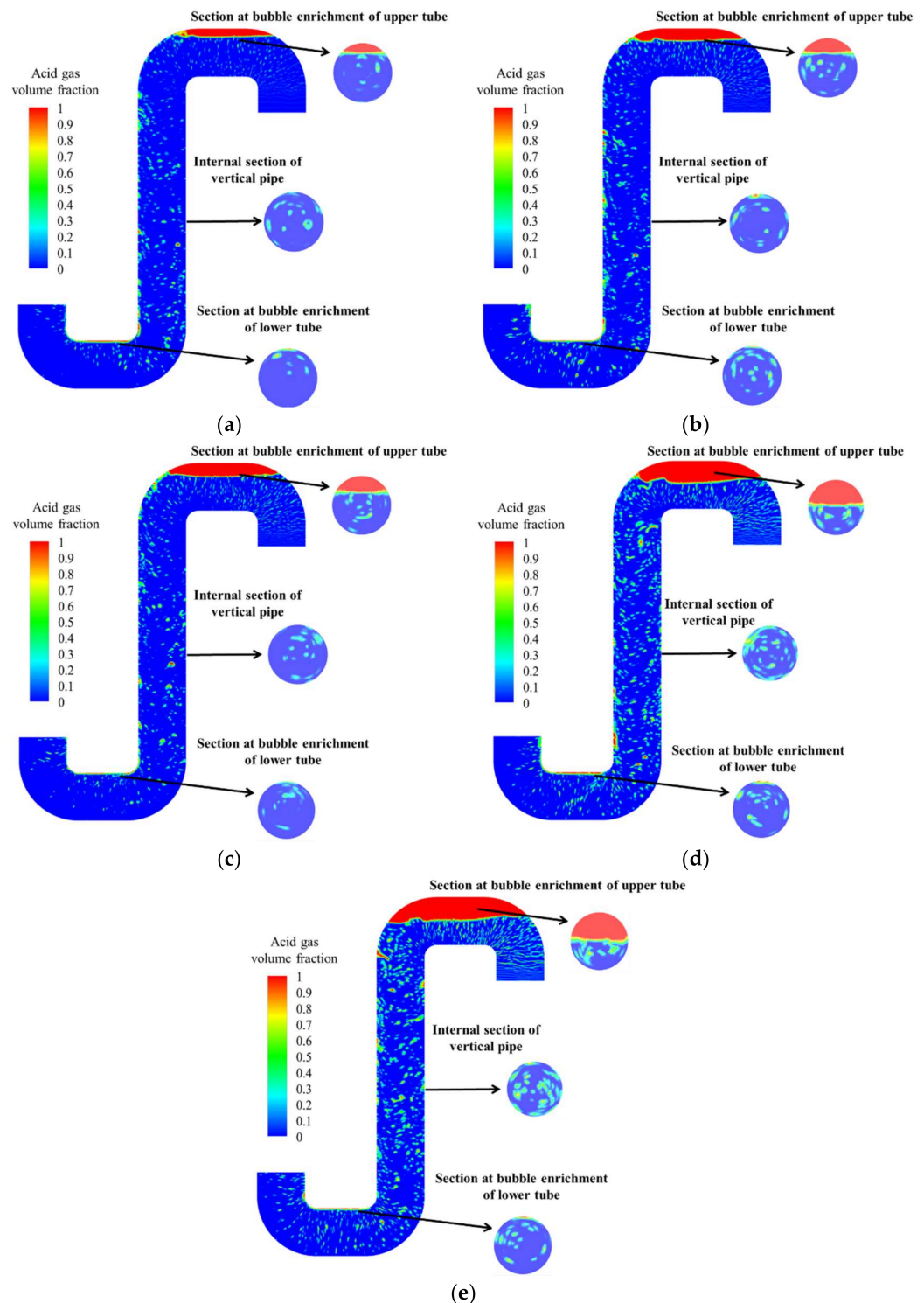


Figure 13. Acid gas phase distribution under different inlet gas fraction conditions ($t = 11$ s, $u = 0.67$ m/s). (a) $\alpha = 0.03$ (b) $\alpha = 0.05$ (c) $\alpha = 0.07$. (d) $\alpha = 0.1$ (e) $\alpha = 0.12$.

3.3. Corrosion Characteristics

Due to the high content of CO_2 in acid gas, it has a great impact on pipeline corrosion. Actually, many other factors such as HS_2 , R_2NH , thermally stable salts, Cl^- , and polluted impurities accelerate corrosion. However, the industrial-scale corrosion simulation is still limited due to the lack of corrosion kinetics model, especially for the content of HS_2 . Here, CO_2 is used for gas–liquid two-phase corrosion analysis. The calculation of the corrosion

rate is based on the following assumptions: (1) a stable liquid film is formed on the pipe wall [50], (2) the corrosion rate is affected by the difference in acid gas concentration, (3) all acid gases near the pipe wall participate in the corrosion reaction, and (4) the time effect of corrosion evolution is ignored, that is, the formation and influence of corrosion product films are ignored. Based on the above assumptions, the corrosion rate of the pipe wall is deduced by the mass transfer theory and realized by UDF in the CFD software, and the diffusion equation for calculating the corrosion rate is shown in Appendix A (Appendix A.4).

In simulation, the maximum corrosion rate is obtained by monitoring points along the upper wall of the pipeline. At the same time, the remaining wall thickness was measured by an ultrasonic thickness measuring instrument. The original pipe is 20# steel and its thickness is 13 mm. The smaller the pipe's remaining wall thickness, the more serious the corrosion. The corrosion rate simulation results and the measured remaining wall thickness are shown in Figure 14. The greater the corrosion rate calculated by the simulation, the smaller the wall thickness measured. In Figure 14, the corrosion rates at the points p5 and p10 are much larger, and the wall thicknesses corresponding to the measured points are thinner; that is, the upper part of the elbow R1 and the elbow R2 are easily corroded. The corrosion rates of points p1, p6, and p11 are much lower, and the remaining wall thickness corresponding to the measured points is thicker; that is, at these positions, the corrosion of the pipeline is lighter. The simulated trend of the corrosion is consistent with the actual working conditions. In engineering applications, it is necessary to focus on protecting the outlet section of elbow R1 and inlet section of elbow R2. In these positions, the flow pattern varies from bubbly flow to stratified flow, or it evolves from the stratified flow to bubbly flow, which induces great effect on the gas–liquid interface, fluctuates, and further causes the huge variation of pressure gradient and velocity, enhancing the corrosion mass transfer from the wall to fluid. According to the simulation results, the horizontal section L1 is the bubble enrichment area. It is possible to implement some protective measures to avoid the flow pattern evolution for prolonging the service life of the pipeline of the lean/rich amine liquid heat exchanger.

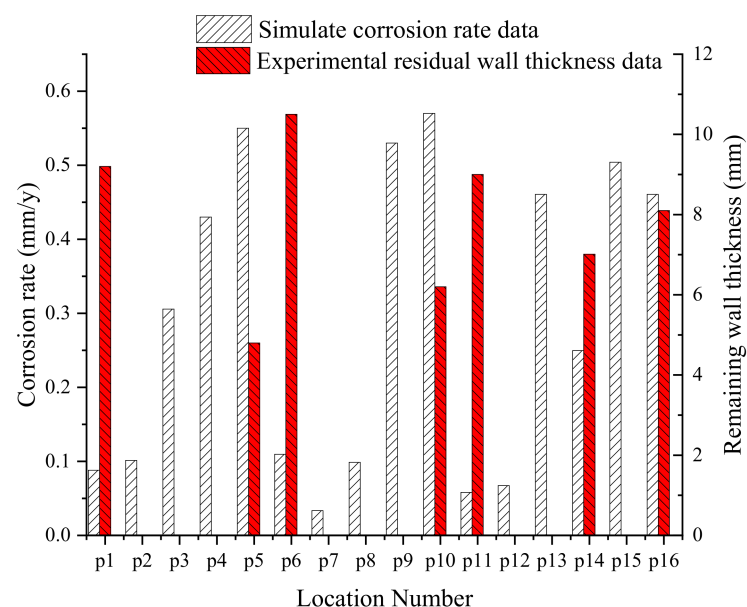


Figure 14. Corrosion rate of monitor points.

4. Anti-Corrosion Treatment

The corrosion of gas–liquid two-phase flow to the pipeline is relatively serious, and the released acid gas will accumulate in the pipeline part. To avoid the pipeline corrosion caused by the accumulation of the pipeline acid gas, reduce the corrosion of the pipeline, and prolong the use of the pipeline, a bifurcated pipe is installed at the upper wall of the horizontal section L1 to achieve the purpose of discharging the acid gas.

Figure 15 shows the position of the bifurcated pipe. The bifurcated pipe is installed near the outlet of elbow R1. The acid gas that was originally collected on the upper wall in the pipe, as shown in Figure 15a, can be discharged out of the pipe through the bifurcated pipe, as shown in Figure 15b–d. The air bubbles existing in the rest of the pipe also move toward the direction of the bifurcated pipe. Three inner diameters of the bifurcated pipe including 300 mm, 500 mm and $D = 600$ mm were simulated. With the increase in bifurcated pipe diameter, the bubble number in the vertical section L3 is greatly reduced. Figure 15e evaluates the acid gas separation efficiency. The separation efficiency of the three bifurcated pipes is similar to each other. However, a larger bifurcated pipe means a much more amine bypassing. It suggests to choose a bifurcated pipe with a diameter of 500 mm, 300 mm or smaller according to the acid gas holdup. Figure 16 shows that the stratified flow in the horizontal section L1 can be eliminated after adding the bifurcated pipe where the gas fraction varies from 0.03 to 0.12. It is found through the cloud map that this method has the obvious effect of eliminating stratified flow, which is beneficial for protecting the pipeline.

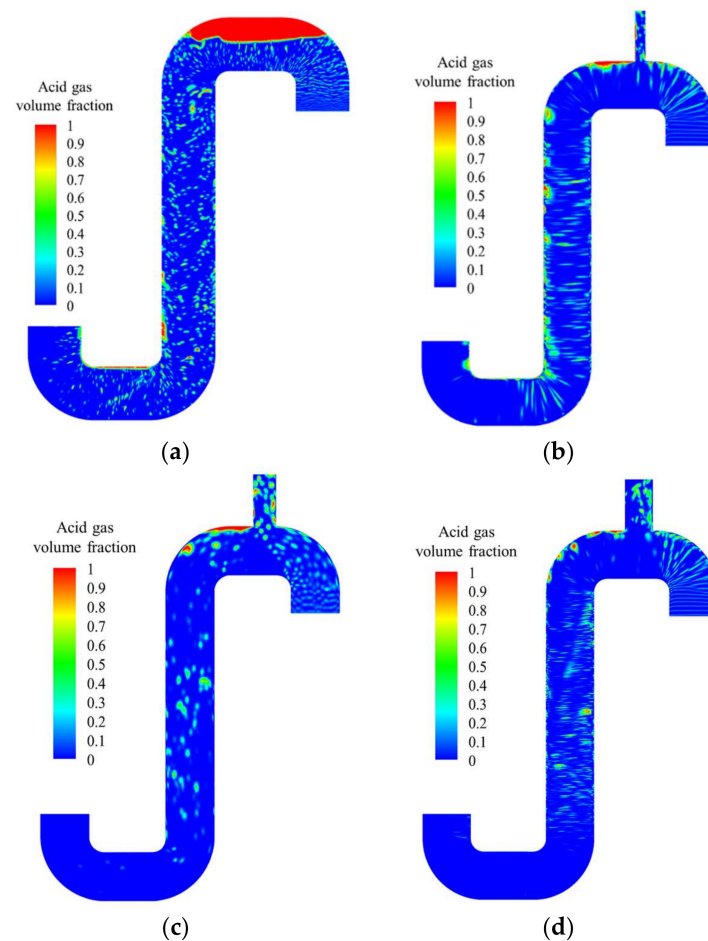
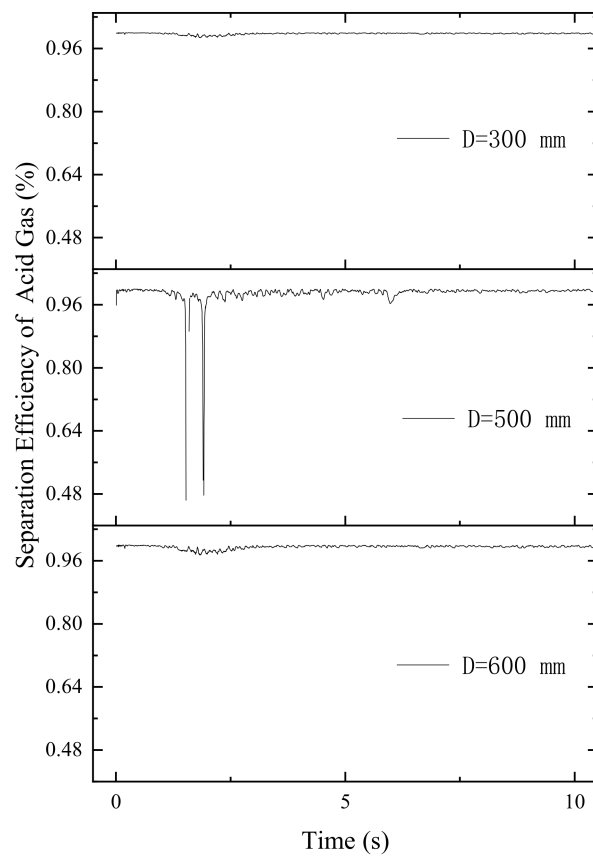


Figure 15. Cont.



(e)

Figure 15. Gas phase distribution with a volume fraction of 0.1 ($t = 11$ s, $u = 0.67$ m/s). (a) Without bifurcated pipe (b) With bifurcated pipe of diameter 300 mm. (c) With bifurcated pipe of diameter 500 mm (d) With bifurcated pipe of diameter 600 mm. (e) Acid gas separation efficiency with variable bifurcated pipe diameter.

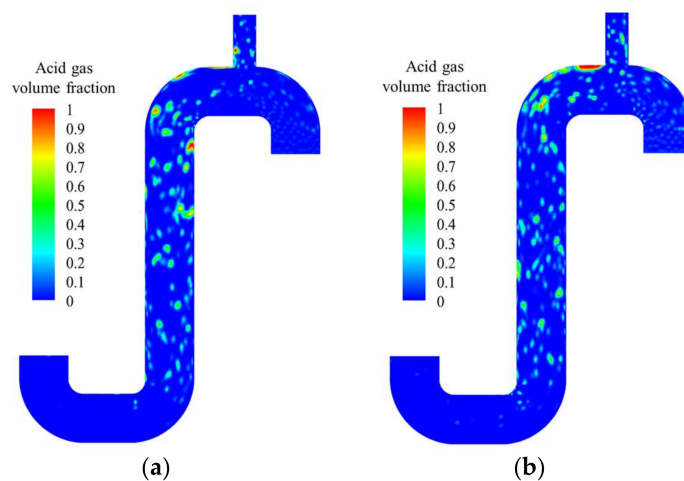


Figure 16. Cont.

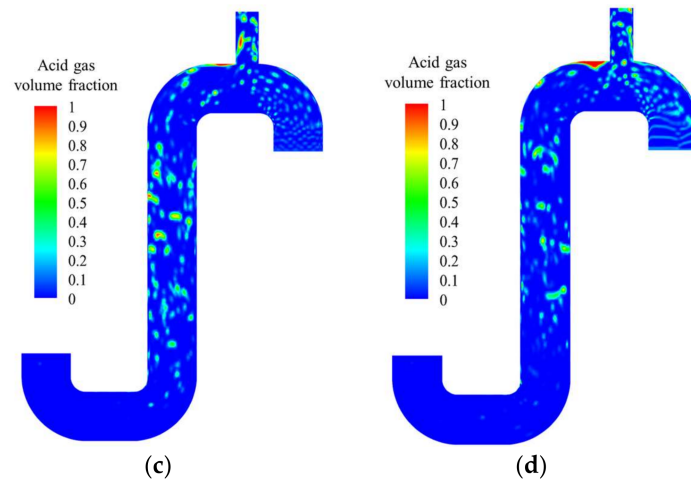


Figure 16. Gas phase distribution at different volume fractions (diameter of bifurcated pipe is 500 mm, $t = 11$ s, $u = 0.67$ m/s. (a) $\alpha = 0.03$ (b) $\alpha = 0.05$ (c) $\alpha = 0.07$. (d) $\alpha = 0.12$.

According to the cloud map of gas phase distribution under different working conditions, Figure 17 compares the volume fraction of acid gas at the inlet and the bifurcated pipe, and it calculates the time-dependent acid gas separation efficiency diagram for the corresponding working conditions as shown below. When the acid gas volume fraction is 0.12 and the time is 2.005 s, the gas–liquid separation efficiency of acid gas fluctuates to a much larger extent, and then, the separation efficiency tends to be stable and close to 100%. When the acid gas volume fraction is 0.03, the separation efficiency of acid gas fluctuates in an narrow range, and the separation efficiency is mostly concentrated at about 99.6%, which indicates a good separation efficiency. Therefore, using the bifurcated pipe can well complete the gas–liquid separation of the pipeline.

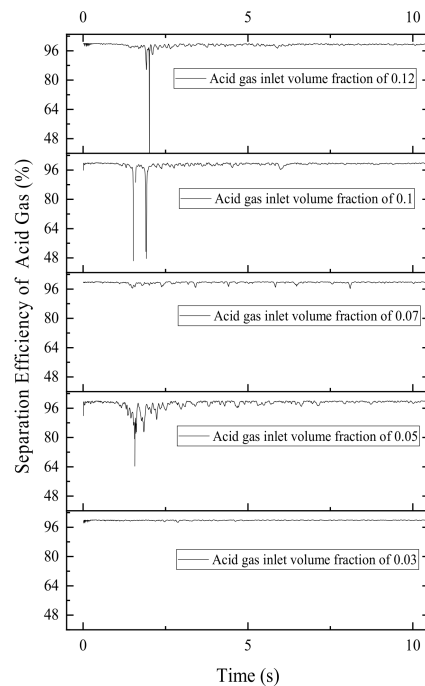


Figure 17. Variation of acid gas separation efficiency for bifurcated pipe with diameter of 500 mm.

5. Conclusions

In this paper, the acid gas and amine liquid two-phase flow and corrosion process in the connecting pipe of a lean/rich amine heat exchanger for natural gas purification is numerically simulated. The effect of acid gas fraction on the flow and corrosion characteristics was investigated in detail, and a method of adding bifurcated pipe was proposed to help reduce the acid gas accumulation in the horizontal section. The conclusions mainly include the following:

(1) A full-scale numerical model was developed to simulate the gas–liquid flow in the connecting pipe of a lean/rich amine heat exchanger and validated by comparing with the experimental data in terms of bubbling pattern and gas film thickness. The flow pattern of the connecting pipe of a lean/rich amine heat exchanger is complex and obviously diverged in each section. The elbow sections and vertical section show a typical bubbly flow, while the horizontal section shows stratified flow. The increase in the gas holdup increases the gas film thickness and enlarges the bubble diameter in the elbow sections and vertical section.

(2) The increasing acid gas fraction causes a much larger pressure drop, increases the local velocity, enlarges the high-pressure area, and promotes gas enrichment in the horizontal section L1 and the proportion of bubbles in each section. The maximum pressure gradient is located at the lower wall of the vertical section L2. The increasing acid gas fraction gradually increases the local velocity and decreases the section area of low flow rate. The maximum velocity in the pipe is concentrated in elbow R4.

(3) The variation trend of corrosion rate predicted by the present model is consistent with the measured value. The method of welding the bifurcated pipe at the acid gas enrichment point can discharge the originally enriched acid gas on the upper wall of the pipeline through the manifold, reduce the acid gas content in the main pipeline, and thus reduce the corrosion to the pipeline.

Author Contributions: Data collection and writing, Z.S.; figures and data analysis, J.L. and Z.E.; data collection, P.W. and Y.G.; data analysis, Y.L.; study design, W.S. and Y.Y.; data interpretation and writing, L.W.; literature search, J.H. All authors have read and agreed to the published version of the manuscript.

Funding: This research was funded by the National Natural Science Foundation of China (No. 22278332) and the Science and Technology Plan Project of Petro China Southwest Oil & Gasfield Company (No. 20210310-10).

Institutional Review Board Statement: Not applicable.

Informed Consent Statement: Not applicable.

Data Availability Statement: All data that support the findings of this study are included within the article.

Conflicts of Interest: The authors declare no conflict of interest.

Appendix A

Appendix A.1. Governing Equations

The continuity equation for the volume fraction of acid gas is shown as follows [51]:

$$\frac{\partial \rho_o \alpha_o}{\partial t} + \nabla \cdot (\rho_o \alpha_o \mathbf{u}) = 0 \quad (\text{A1})$$

where \mathbf{u} is the velocity vector, m/s; ρ_o is the acid gas density, kg/m³; α_o is the volume fraction value of acid gas [52]. If $\alpha_o = 0$, it means that the calculation unit is all MDEA phase without gas phase; if $0 < \alpha < 1$, it means that the calculation unit contains both acid gas and MDEA phases; if $\alpha = 1$, it means that the phase is all acid gas phase.

The volume fractions of all phases sum to unity in each control volume:

$$\sum \alpha = 1 \quad (\text{A2})$$

The volume fraction Equation (A1) is only solved for acid gas, and the volume fraction of MDEA phases is calculated by Equation (A4).

The mixture momentum equation is solved as follows.

$$\frac{\partial(\rho u)}{\partial t} + \nabla \cdot (\rho u u) = -\nabla P + \rho g + \left[\mu (\nabla u + \nabla u^T) \right] + F \quad (A3)$$

where ρ is the volume-fraction-weighted density, kg/m^3 ; μ is the volume-fraction-weighted viscosity of the mixture, $\text{Pa}\cdot\text{s}$; P is the pressure, Pa ; g is the acceleration of gravity, m/s^2 ; and F is the surface tension force, N/m . The interaction process of the gas–liquid interface can be solved based on the VOF model, especially the gas-phase exfoliation process under the action of strong shear.

The continuum surface force (CSF) model [53] is applied to calculate F in Equation (A3):

$$F = \sigma \frac{\rho \kappa_m \nabla \alpha_m}{\frac{1}{2}(\rho_m + \rho_o)} \quad (A4)$$

where κ_m is defined in terms of the divergence of the unit normal; σ is the surface tension coefficient, which is set as 0.007 [17]. α_m is the volume fraction of the MDEA phase, and ρ_m is the density of the MDEA phase, kg/m^3 .

Appendix A.2. Discretization Method

Appendix A.2.1. Time Terms

The time terms in Equations (A1) and (A3) are discretized by an explicit time-marching scheme. The time step is set as 0.01 s for keeping a suitable Courant number and quick iteration. The volume fraction is updated in each time step.

Appendix A.2.2. Discretization of the Volume Fraction Equation

The volume fraction equation is solved through explicit time formulation:

$$\frac{\alpha_o^{n+1} \rho_o^{n+1} - \alpha_o^n \rho_o^n}{\Delta t} V + \sum_f (\rho_o U_f^n \alpha_{o,f}^n) = 0 \quad (A5)$$

In Equation (A5), $n + 1$ means index for new (current) time step; n is index for previous time step; $\alpha_{o,f}$ is the face value of the acid gas volume fraction; V is the volume of cell; and U_f is volume flux through the face in the normal direction. The explicit scheme calculates the current volume fraction by the previous time step, which is easily obtained without iteration. The face fluxes U_f is interpolated by Geo-Reconstruct schemes [54].

Appendix A.2.3. Discretization of the Momentum Equation

The momentum equation is assembled to a linear matrix by applying the grid volume integral and Gaussian transformation. The convection term and diffusion terms of the momentum equation are discretized by a second upwind scheme [55]. The gradient terms are calculated by Least Squares Cell-Based Gradient Evaluation [56]. The pressure term is computed by the PRESTO! method [57].

The matrix formula for computing the velocity in each cell is set:

$$a_p u = \sum_{nb} a_{nb} u_{nb} + \sum p_f A + S \quad (A6)$$

where u_{nb} is the velocity value in neighbor cells, p_f is the mass flux across the interface between the owner and neighbor cell, A is the surface vector of the interface between the owner and neighbor cell, S is the source terms; and a_p and a_{nb} are the coefficients of the owner and neighbor cell, respectively, which is determined by the discretization schemes and the interpolation method. If the pressure field and face mass fluxes are known, Equation (A6) can be solved in the manner outlined in discretization.

Appendix A.3. Turbulence Model

The gas–liquid flow in the pipeline is a typical turbulent flow [8]. In the standard $k - \varepsilon$ model, the specific equation is as follows:

$$\frac{\partial}{\partial t}(\rho k) + \frac{\partial}{\partial x_i}(\rho k u_i) = \frac{\partial}{\partial x_j} \left[\left(\mu + \frac{\mu_t}{\sigma_k} \right) \frac{\partial k}{\partial x_j} \right] + G_k + G_b - p\varepsilon - Y_M + S_k \quad (A7)$$

$$\frac{\partial}{\partial t}(\rho \varepsilon) + \frac{\partial}{\partial x_i}(\rho \varepsilon u_i) = \frac{\partial}{\partial x_j} \left[\left(\mu + \frac{\mu_t}{\sigma_\varepsilon} \right) \frac{\partial \varepsilon}{\partial x_j} \right] + C_{1\varepsilon} \frac{\varepsilon}{k} \left(\vec{J}_k + C_{3\varepsilon} G_b \right) - C_{2\varepsilon} \rho \frac{\varepsilon^2}{k} + S_\varepsilon \quad (A8)$$

where G_k is the turbulent kinetic energy generated by the average velocity gradient, G_b is the turbulent kinetic energy generated by buoyancy, Y_M is the effect of pulsating expansion of compressible turbulence on total dissipation, μ_t is turbulent viscosity; $\sigma_k, \sigma_\varepsilon$ represent the Prandtl number of turbulent kinetic energy and turbulent energy dissipation rate, respectively, where $\sigma_k = 1.3, \sigma_\varepsilon = 1.0$. $C_{1\varepsilon}, C_{2\varepsilon}, C_{3\varepsilon}$ is the empirical constant; $C_{1\varepsilon} = 1.44, C_{2\varepsilon} = 1.92$, and $C_{3\varepsilon} = 0.09$. S_k, S_ε is the source item.

And:

$$\mu_{eff} = \mu + \mu_t \quad (A9)$$

$$\mu_t = \rho C_\mu \frac{k^2}{\varepsilon} \quad (A10)$$

where μ_{eff} is the effective viscosity, m/s; μ_t is turbulent viscosity; and the value of C_μ is 0.0845 [58,59].

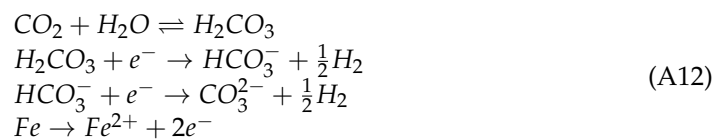
Appendix A.4. Diffusion Equation for Calculating Corrosion Rate

The diffusion flux of CO_2 on adjacent walls can be expressed as:

$$J_{\text{CO}_2} = D_m \cdot \left(\frac{dC}{dy} \right)_y = D_m \cdot \frac{C_b - C_w}{\delta_d} \quad (A11)$$

where D_m is the mass transfer coefficient, m^2/s ; C_b is the body fluid concentration, mol/m^3 ; C_w is the wall concentration, mol/m^3 ; δ_d is the thickness of boundary layer, m; and J_{CO_2} is the CO_2 diffusion flux, $\text{mol}/(\text{m}^2 \cdot \text{s})$.

According to the chemical reaction equation of CO_2 corrosion:



The flux of Fe on the metal surface is $J_{\text{Fe}^{2+}} = J_{\text{CO}_2}$. Therefore, the corrosion rate CR can be expressed as:

$$\text{CR} = \frac{J_{\text{Fe}^{2+}} M_{\text{Fe}}}{\rho_{\text{Fe}}} \quad (A13)$$

As mentioned above, the CO_2 concentration distribution near the wall can be obtained by calculating the volume fraction of CO_2 .

$$C_{\text{CO}_2} = \frac{n_{\text{CO}_2}}{V} = \frac{m_{\text{CO}_2}}{M_{\text{CO}_2} V} = \frac{\rho_{\text{CO}_2} \cdot V \cdot v_{\text{CO}_2} \%}{M_{\text{CO}_2} \cdot V} = \frac{\rho_{\text{CO}_2} \cdot v_{\text{CO}_2} \%}{M_{\text{CO}_2}} \quad (A14)$$

In Equation (A14), V is the unit volume of the calculation grid; $v_{\text{CO}_2} \%$ is the volume fraction of CO_2 in cells. In Equation (A11), the diffusion coefficient D_m (m^2/s) of CO_2

in water is calculated by the Wilke–Chang formula. The result of Equation (A15) can be brought into Equation (A11) for calculation:

$$D_d = 7.4 \times 10^{-15} \times \frac{T(\beta M_{H_2O})^{0.5}}{\eta_{H_2O} v_{CO_2}^{0.6}} \quad (A15)$$

In Equation (A15), T is the temperature, K; β is the solvent formation coefficient (under the condition of water solvent, $\beta = 2.6$), M_{H_2O} is the molar mass of water, which is 18 g/mol; η_{H_2O} is the dynamic viscosity of water, Pa · s; and v_{CO_2} is the molar volume of CO₂ solute [60].

References

- Ou, G.; Bie, K.; Zheng, Z.; Shu, G.; Wang, C.; Cheng, B. Numerical simulation on the erosion wear of a multiphase flow pipeline. *Int. J. Adv. Manuf. Technol.* **2018**, *96*, 1705–1713. [\[CrossRef\]](#)
- De Waard, C.; Lotz, U.; Milliams, D.E. Predictive model for CO₂ corrosion engineering in wet natural gas pipelines. *Corrosion* **1991**, *47*, 976–985. [\[CrossRef\]](#)
- Xiao, R.; Han, S.; Lyu, T. Research on corrosion and protection for gas-liquid two-phase pipeline. *Hot Work. Technol.* **2015**, *44*, 64–67.
- Qin, M.; Liao, K.; Zhu, W.; Huang, X.; An, C.; Zhou, W. Gas Liquid Interface Corrosion Behavior of X65 Steel in CO₂ and H₂S Corrosive. *Mater. Prot.* **2022**, *55*, 33–40.
- Liao, K.; Qin, M.; He, G.; Yang, N.; Zhang, S. Study on corrosion mechanism and the risk of the shale gas gathering pipelines. *Eng. Fail. Anal.* **2021**, *128*, 105622. [\[CrossRef\]](#)
- Liu, J.; BaKeDaShi, W.; Li, Z.; Xu, Y.; Ji, W.; Zhang, C.; Cui, G.; Zhang, R. Effect of flow velocity on erosion corrosion of 90-degree horizontal elbow. *Wear Int. J. Sci. Technol. Frict. Lubr. Wear* **2017**, *376–377*, 516–525. [\[CrossRef\]](#)
- Zheng, D.; Che, D.; Liu, Y. Experimental investigation on gas-liquid two-phase slug flow enhanced carbon dioxide corrosion in vertical upward pipeline. *Corros. Sci.* **2008**, *50*, 3005–3020. [\[CrossRef\]](#)
- Zheng, D.; He, X.; Che, D. CFD simulations of hydrodynamic characteristics in a gas-liquid vertical upward slug flow. *Int. J. Heat Mass Transf.* **2007**, *50*, 4151–4165. [\[CrossRef\]](#)
- Nešić, S.; Kahyarian, A.; Choi, Y.S. Implementation of a comprehensive mechanistic prediction model of mild steel corrosion in multiphase oil and gas pipelines. *Corrosion* **2019**, *75*, 274–291. [\[CrossRef\]](#)
- Magnini, M.; Ullmann, A.; Brauner, N.; Thome, J. Numerical study of water displacement from the elbow of an inclined oil pipeline. *J. Pet. Sci. Eng.* **2018**, *166*, 1000–1017. [\[CrossRef\]](#)
- Haghtalab, A.; Shojaeian, A. Modeling solubility of acid gases in alkanolamines using the nonelectrolyte Wilson-nonrandom factor model. *Fluid Phase Equilibria* **2010**, *289*, 6–14. [\[CrossRef\]](#)
- Wang, K.; Li, C.; Lu, J.; Nan, C.; Zhang, Q.; Zhang, H. Intelligent Evaluation of Marine Corrosion of Q420 Steel Based on Image Recognition Method. *Coatings* **2022**, *12*, 881. [\[CrossRef\]](#)
- Hu, J.; Wang, T.; Wang, Z.; Wei, L.; Zhu, J.; Zheng, M.; Chen, Z. Corrosion protection of N80 steel in hydrochloric acid medium using mixed C₁₅H₁₅NO and Na₂WO₄ inhibitors. *Coatings* **2018**, *8*, 315. [\[CrossRef\]](#)
- Duan, Y.F.; Miao, P.; Yu, F.C. Corrosion Failure Analysis of Lean / Rich Amine Heat Exchanger in Natural Gas Purification Unit. *Corros. Prot. Petrochem. Ind.* **2014**, *31*, 61–64.
- Duan, Y.F.; Zhang, J.; Zong, R.L.; Zhao, X.Y. Study on the Cause and Corrosion Behavior of Heat Stable Salt in Natural Gas Purification Process. *Corros. Prot. Petrochem. Ind.* **2018**, *35*, 1–7.
- Zhao, Y.L. Study on Gas-Liquid Two-Phase Flow Characteristics in the Gas Pipeline. Master's Thesis, China University of Petroleum (East China), Dongying, China, 2017.
- Yang, Y.X. Study on Oil-Water Two-Phase Flow Characteristics in Light Crude Oil Pipeline. Master's Thesis, Southwest Petroleum University, Chengdu, China, 2018.
- Zhang, H.; Lan, H.; Lin, N. A numerical simulation of water distribution associated with internal corrosion induced by water wetting in upward inclined oil pipes. *J. Pet. Sci. Eng.* **2019**, *173*, 351–361. [\[CrossRef\]](#)
- Banat, F.; Younas, O.; Didarul, I. Energy and exergical dissection of a natural gas sweetening plant using methyldiethanol amine (MDEA) solution. *J. Nat. Gas Sci. Eng.* **2014**, *16*, 1–7. [\[CrossRef\]](#)
- Faramawy, S.; Zaki, T.; Sakr, A.A.E. Natural gas origin, composition, and processing: A review. *J. Nat. Gas Sci. Eng.* **2016**, *34*, 34–54. [\[CrossRef\]](#)
- Zheng, Y.; Ning, J.; Brown, B.; Nesic, S. Advancement in predictive modeling of mild steel corrosion in CO₂-and H₂S-containing environments. *Corrosion* **2016**, *72*, 679–691. [\[CrossRef\]](#)
- Gourari, S.; Mebarek-Oudina, F.; Makinde, O.D.; Rabhi, M. Numerical investigation of Gas-Liquid Two-Phase flows in a cylindrical channel. *Defect Diffus. Forum* **2021**, *409*, 39–48. [\[CrossRef\]](#)
- Zhang, Q.; He, W.; Yang, X.; Liu, S. Analysis on Fluid-solid Coupling Characteristics of Gas-liquid Two-phase Flow Corrosion Pipeline. *Therm. Process. Technol.* **2021**, *50*, 38–42.

24. Chunsheng, W.; Zejun, L.; Yan, Z.; Qiji, S. Study on Characteristics of Flow-induced Vibration (FIV) Induced by Gas-liquid Two-phase Flow in the Conveying Pipe. *Int. J. Multiphys.* **2020**, *14*, 17–30.
25. Feng, J.; Wu, C.; Zhang, J.; Qin, C.; Chen, Z. Effect of Iron Ion on the Evaluation of Buried-Steel Pipeline Corrosion. *J. Mater. Civ. Eng.* **2022**, *34*, 04022019. [[CrossRef](#)]
26. Iftikhar, A.; Rahuma, N.M. Corrosion mitigation and inspection strategy for pipeline integrity management: An experience of Sarir Oilfield. *Corrosion* **2013**, *2013*, 2249.
27. Thakur, A.K.; Arya, A.K.; Sharma, P. Analysis of cathodically protected steel pipeline corrosion under the influence of alternating current. *Mater. Today Proc.* **2022**, *50*, 789–796. [[CrossRef](#)]
28. Paolinelli, L.D.; Nestic, S. Calculation of mass transfer coefficients for corrosion prediction in two-phase gas-liquid pipe flow. *Int. J. Heat Mass Transf.* **2021**, *165*, 120689. [[CrossRef](#)]
29. Yang, G.; Zhu, Z.; Song, W.; Li, Y.; Ma, Y. Corrosion behavior of 20# steel at initial stage under the (CO₂/aqueous solution) gas-liquid two-phase plug flow condition. *Mater. Res. Express* **2019**, *6*, 066512.
30. Peng, S.; Zhang, Z.; Liu, E.; Liu, W.; Qiao, W. A new hybrid algorithm model for prediction of internal corrosion rate of multiphase pipeline. *J. Nat. Gas Sci. Eng.* **2021**, *85*, 103716. [[CrossRef](#)]
31. Li, P. Study on Gas/Liquid Two Phase Flow of Flow- accelerated Corrosion and Simulation with CFD Method. *Chem. Manag.* **2014**, 163–165. [[CrossRef](#)]
32. Hirt, C.W.; Nichols, B.D. Volume of fluid (VOF) method for the dynamics of free boundaries. *J. Comput. Phys.* **1981**, *39*, 201–225. [[CrossRef](#)]
33. Samkhaniani, N.; Ansari, M.R. Numerical simulation of bubble condensation using CF-VOF. *Prog. Nucl. Energy* **2016**, *89*, 120–131. [[CrossRef](#)]
34. Lafmejani, S.S.; Olesen, A.C.; Kær, S.K. VOF modelling of gas-liquid flow in PEM water electrolysis cell micro-channels. *Int. J. Hydrog. Energy* **2017**, *42*, 16333–16344. [[CrossRef](#)]
35. Yaqub, M.W.; Pendyala, R. CFD simulations of gas-liquid-liquid three-phase co-current flow in horizontal pipe by tracking volume fractions using VOF model. In *IOP Conference Series: Materials Science and Engineering*; IOP Publishing: Bristol, UK, 2018; Volume 458, p. 012078.
36. Yang, G.; Song, W.; Wang, F.; Ma, Y.; Hao, Y. Corrosion behavior of 20# steel in aqueous CO₂ solution under stratified gas-liquid two-phase flow condition. *Anti-Corros. Methods Mater.* **2018**, *66*, 11–18.
37. Savović, S.; Djordjević, A.; Ristić, G. Numerical solution of the transport equation describing the radon transport from subsurface soil to buildings. *Radiat. Prot. Dosim.* **2012**, *150*, 213–216. [[CrossRef](#)] [[PubMed](#)]
38. Zhou, H.Y.; Wang, A.M. Research on adaptive methods of non-linear partial micro-division value solution. *Comput. Eng. Appl.* **2011**, *47*, 38–40.
39. Groza, G.; Razzaghi, M. Approximation of solutions of polynomial partial differential equations in two independent variables. *J. Comput. Appl. Math.* **2019**, *346*, 205–223. [[CrossRef](#)]
40. Li, C.; Chen, A. Numerical methods for fractional partial differential equations. *Int. J. Comput. Math.* **2018**, *95*, 1048–1099. [[CrossRef](#)]
41. Yavneh, I.; Dardyk, G. A multilevel nonlinear method. *SIAM J. Sci. Comput.* **2006**, *28*, 24–46. [[CrossRef](#)]
42. Hajipour, M.; Jajarmi, A.; Baleanu, D.; Sun, H. On an accurate discretization of a variable-order fractional reaction-diffusion equation. *Commun. Nonlinear Sci. Numer. Simul.* **2019**, *69*, 119–133. [[CrossRef](#)]
43. Barth, T.; Ohlberger, M. Finite Volume Methods: Foundation and Analysis. 2003. Available online: <https://ntrs.nasa.gov/api/citations/20030020790/downloads/20030020790.pdf> (accessed on 23 September 2022).
44. Moukalled, F.; Mangani, L.; Darwish, M. The finite volume method. In *The Finite Volume Method in Computational Fluid Dynamics*; Springer: Cham, Switzerland, 2016; pp. 103–135.
45. Eymard, R.; Gallouët, T.; Herbin, R. Finite volume methods. In *Handbook of Numerical Analysis*; Elsevier: Amsterdam, The Netherlands, 2000; Volume 7, pp. 713–1018.
46. Mencinger, J.; Žun, I. On the finite volume discretization of discontinuous body force field on collocated grid: Application to VOF method. *J. Comput. Phys.* **2007**, *221*, 524–538. [[CrossRef](#)]
47. Garoosi, F.; Hooman, K. Numerical simulation of multiphase flows using an enhanced Volume-of-Fluid (VOF) method. *Int. J. Mech. Sci.* **2022**, *215*, 106956. [[CrossRef](#)]
48. Li, D. The Corrosion Mechanism of 20# Steel in CO₂/H₂O Two Phase Bubble Flow and Its Forecast Model. Master's Thesis, Lanzhou University of Technology, Lanzhou, China, 2018.
49. Qiao, S.; Kim, S. Air-water two-phase bubbly flow across 90° vertical elbows. Part I: Experiment. *Int. J. Heat Mass Transf.* **2018**, *123*, 1221–1237. [[CrossRef](#)]
50. Liu, W.H.; Li, W.S.; Lyu, N.X.; Fu, A.Q.; Ma, Q.R. Simulation of Gas-Liquid Two-Phase Flow-Induced Corrosion at Premium Connection in High Productivity Gas Wells Containing CO₂. *Mater. Sci. Forum* **2020**, *993*, 1196–1202. [[CrossRef](#)]
51. Shi, J.; Gourma, M.; Yeung, H. CFD simulation of horizontal oil-water flow with matched density and medium viscosity ratio in different flow regimes. *J. Pet. Sci. Eng.* **2017**, *151*, 373–383. [[CrossRef](#)]
52. Fan, X.H. Numerical Simulation and Control Method of Gas-Liquid-Solid Three-Phase Flow Mixture Based on VOF-DEM. Master's Thesis, Zhejiang University of Technology, Zhejiang, China, 2021.

53. Brackbill, J.U.; Kothe, D.B.; Zemach, C. A Continuum Method for Modeling Surface Tension. *J. Comput. Phys.* **1992**, *100*, 335–354. [[CrossRef](#)]
54. Youngs, D.L. Time-Dependent Multi-Material Flow with Large Fluid Distortion. In *Numerical Methods for Fluid Dynamics*; Morton, K.W., Baines, M.J., Eds.; Academic Press: Cambridge, MA, USA, 1982.
55. Wu, D.Z.; Huang, B.; Hu, F.F.; Wu, P.; Wang, L.Q. Numerical simulation on a centrifugal pump under different discrete scheme. *J. Eng. Thermophys.* **2012**, *33*, 55–58.
56. Zhao, H.; Zhang, Y.B.; Chen, J.T.; Deng, Y.Q. The accuracy assessment of gradient computation methods on unstructured grids. *J. Acta Aerodyn. Sin.* **2019**, *37*, 844–854.
57. Tan, Y.F.; Dong, G.Y.; Tan, H.G.; Tan, H.; Wang, X.L. Numerical Simulation of Rotating Self-cleaning Air Pre-Filter Based on Computational Fluid Dynamics. *J. Mil. Eng.* **2014**, *35*, 409–414.
58. Issakhov, A.; Bulgakov, R.; Zhandaulet, Y. Numerical simulation of the dynamics of particle motion with different sizes. *Eng. Appl. Comput. Fluid Mech.* **2019**, *13*, 1–25. [[CrossRef](#)]
59. Yang, J.; Teng, P.; Zhang, H. Experiments and CFD modeling of high-velocity two-phase flows in a large chute aerator facility. *Eng. Appl. Comput. Fluid Mech.* **2019**, *13*, 48–66. [[CrossRef](#)]
60. Wilke, C.R.; Chang, P. Correlation of diffusion coefficients in dilute solutions. *AIChE J.* **1955**, *1*, 264–270. [[CrossRef](#)]